Dynamic Behavior of an Ordinary Chondrite: the Effects of Microstructure on Strength, Failure and Fragmentation

James David Hogan[a,b], Jamie Kimberley[c], Kavan Hazeli[b], Jeffrey Plescia[d], KT Ramesh[b]

[a]*Department of Mechanical Engineering, The University of Alberta, Edmonton, AB T6G 2R3, Canada*
[b]*Hopkins Extreme Materials Institute, The Johns Hopkins University, Baltimore, MD 21218, USA*
[c]*New Mexico Institute of Mining and Technology, Soccoro, NM 87801*
[d]*Applied Physics Laboratory, The Johns Hopkins University, Laurel, Maryland 20723*

Abstract

Knowledge of the relationships between microstructure, stress-state and failure mechanisms is important in the development and validation of numerical models simulating large-scale impact events. In this study, we investigate the effects of microstructural constituent phases and defects on the compressive and tensile strength, failure, and fragmentation of a stony meteorite (GRO 85209). In the first part of the paper we consider the effect of defects on the strength and failure. Strengths are measured and linked with detailed quantification of the important defects in this material. We use the defect statistic measurements in conjunction with our current understanding of rate-dependent strengths to discuss the uniaxial compressive strength measurements of this ordinary chondrite with those of another ordinary chondrite, with a different defect population. In the second part of the paper, we consider the effects of the microstructure and defects on the fragmentation of GRO 85209. Fragment size distributions are measured using image processing techniques and fragments were found to result from two distinct fragmentation mechanisms. The first is a mechanism that is associated with relatively

Email address: jdhogan@ualberta.ca (James David Hogan)

smaller fragments arising from individual defect grains and the coalescence of fractures initiating from microstructure defects. This mechanism becomes more dominant as the strain-rate is increased. The second mechanism is associated with larger fragments that are polyphase and polygrain in character and is dependent on the structural failure mechanisms that are activated during load. In turn, these are dependent on (for example) the strain-rate, stress state, and specimen geometry. The implications of these results are briefly discussed in terms of regolith generation on airless bodies.

Keywords: brittle fragmentation; brittle failure; strength; planetary materials; catastrophic disruption;

---

1. Introduction

Understanding the dynamic behavior of planetary materials in well-controlled laboratory experiments is important when interpreting large-scale impacts (e.g., Hörz and Cintala, 1997) and developing sophisticated numerical models for such dynamic events (e.g., Michel et al., 2003). During impacts, the colliding bodies will experience a range of stress states (compression, tension, shear) and a wide range of strain rates. The stress-state, strain-rate and loading histories determine the failure mechanisms that are activated during impact (Ramesh et al., 2015). Ultimately, we are interested in developing simple physics-based models for strength and fragmentation of planetary materials that take into account these stress-state and strain-rate dependent mechanisms. These simple models can be used to understand the effect of target material and impact conditions on regolith formation and catastrophic disruption, aspects that have been well-studied experimentally (Durda and Flynn, 1999; Flynn and Durda, 2004; Cintala and Hörz, 2008)

Planetary materials are typically quasi-brittle and inhomogeneous, and may be comprised of mineral and metal grains and amorphous clasts, each with varying crystal properties (e.g., structure, size, and shape) and mechanical properties (e.g., density, strength, fracture toughness). Failure in such heterogeneous materials is initiated from internal defects, and this may include grain boundaries, pores, inclusions, and, at much larger scales, faults. The types of defects that are activated are dependent on the loading history (e.g., stress-state and strain-rate) of the event of interest. Commonly, the failure strength of planetary materials exhibits a dependence on strain rate (Kimberley and Ramesh, 2011). Below a critical strain rate, the strength remains nearly constant, but when loaded above this transition strain rate, the strength increases more rapidly for increasing strain rate. The size of the body, the defect density (#/m^3), the degree to which defects are distributed throughout the body, and defect size and orientation distributions have been shown to be important in governing the failure strength of brittle materials (Housen and Holsapple, 1999; Paliwal et al., 2008; Holsapple, 2009; Hu et al., 2014). For example, materials with larger defects have lower strengths than those with smaller defects (for those with the same defect densities). Similarly, materials with more defects are weaker than those with fewer defects (Kimberley et al., 2013). Recently, Kimberley et al. (2013) developed a scaling relationship for the rate-dependent compressive strength of brittle solids based on defect population, average flaw size and flaw density, given some material properties (such as fracture toughness and Young's modulus). We use insights from this scaling law to explore our experimental results on dynamic strength measurements of ordinary chondrites.

During failure, fractures will grow and coalesce and this results in a distribution of fragment sizes across many length scales, ranging from the structural scale (e.g., order of the body-size) down to the micro-scale (e.g., spacing between defects). Measurements of the fragment size and shapes can offer insight into important physical failure processes. For example, larger fragments (boulders) on Eros have been used to constrain its collisional history (Dombard et al., 2010). The extent to which ”microstructure” (including material composition and defects) has an effect on the fragmentation of planetary materials is not yet well understood. This is also explored here.

In this paper we investigate the role of microstructure, strain-rate and stress-state on the strength, failure and fragmentation of an L6 chondrite meteorite (GRO 85209). This study is partially motivated by the work of Ryan (2000) on asteroid fragmentation, and more recently, the review papers by Zhang and Zhao (2013) on the dynamic behaviour of rocks and Ramesh et al. (2015) on the failure of brittle materials. In this manuscript, we study the material's behavior in uniaxial compression and in indirect tension (using the Brazilian disk technique). We begin by introducing the GRO 85209 microstructure, and describe our methods for quantifying initial defect populations and fragments resulting from our experiments. We then explore two critical areas related to dynamic failure: strength and fragmentation. First, we investigate the relationship between defects and the rate dependent strength of GRO 85209 using defect statistic measurements and the recently developed scaling relation of Kimberley et al. (2013). In particular, we explain differences between the strength measurements of ordinary chondrites GRO 85209 and MAC 88118, the latter of which was studied by Kimberley and Ramesh (2011). Second, we explore the role of defects and microstructure on the fragmentation of GRO 85209, identifying the relative contributions of each GRO 85209 constituent phase to fragmentation. We then seek to use the strength, failure, and fragmentation results to provide insights into regolith formation on airless bodies and catastrophic disruption.

2. Methods and Materials

The strength, failure and fragmentation of an ordinary chondrite meteorite are studied in uniaxial compression for quasi-static and dynamic conditions, and in dynamic indirect tension using the dynamic Brazilian disk technique. Descriptions of the material characteristics and testing methods used in this study follow.

2.1. Material Characteristics

The ordinary chondrite meteorite studied here is Grosvenor Mountains (GRO) 85209, an Antarctic find that is currently held at the Smithsonian Institute. It is an L6 chondrite consisting primarily of low-Ca pyroxene and iron nickel, with some olivine (Grossman, 1994). GRO 85209 also contains chondrules (> 3mm in size), but these were not commonly found at the scale of our tested samples due to their relative size. A polarized thin section image of the GRO 85209 microstructure is shown in Figure 1a. Linda Welzenbach of the Smithsonian Institute is credited with analysis of the thin section. Analysis of the thin sections indicates no major fractures, shock veins or brecciation. Olivine (<300 μm and circular), pyroxene (<150 μm and darker in shade), and iron-nickel (< 500 μm, blocky and dark in color in polarized light) grains are highlighted in Figure 1a. Large olivine grains show only irregular fractures and no undulatory extinction, suggesting a shock stage of S1. An optical microscope image of the GRO 85209 microstructure taken in a reflected light mode is shown in Figure 1b. Here, the iron-nickel grains appear white due to their high reflectivity, and are imbedded in a matrix comprised primarily of the low-Ca pyroxene. No internal fractures are visible, nor are any large olivine grains. The Young's modulus of GRO 85209 is 14 GPa (measured during quasi-static tests using digital image correlation, and compared with strain gage measurements), and it has a density of approximately 3,350 kg/m^3 (measured via Archimedes method) and a porosity of 7%.

2.2. Testing Methods

Cuboidal specimens approximately 3.5 mm x 4 mm and 5.3 mm (loading direction) in dimension were used for the uniaxial compression experiments. The dimensions of the Brazilian disk specimens were 10 mm in diameter and 1.5 mm thick. Quasi-static uniaxial compression experiments were performed with an MTS servo-hydraulic test machine under displacement control at strain rates ranging from 10^{-3} to 10^{0} s^{-1}. The dynamic uniaxial compression and Brazilian disk tests were performed using a Kolsky bar apparatus to achieve a range of strain rates from 10^{1} to 10^{3} s^{-1}. Both the MTS machine and Kolsky bar devices used in this study were also used by Kimberley and Ramesh (2011) in their study on the compressive strength of ordinary chondrite MAC 88118, and details of the experimental setup are discussed therein. MAC 88118 is a stony meteorite found in MacAlpine Hills, Antarctica and also currently held at the Smithsonian Institute. The Brazilian disk test is an indirect technique to measure the tensile strength of brittle materials (Li and Wong, 2013). A schematic of the Brazilian Disk setup is shown in Figure 2. The tensile stress, σ_y, in the specimen is calculated as:

$$\sigma_y = \frac{2P}{\pi D t} \tag{1}$$

where P is the load (N), D is the diameter of the disk (m), and t is the thickness (m). While we take the peak stress measurement from the Brazilian disk test as its ”tensile” strength, we note that the stress-state in the disk is actually quite complex (Ruiz et al., 2000; Swab et al., 2011), and thus the specimen undergoes non-uniform deformation. This will be taken into consideration in the interpretation of our fragmentation results. Please refer to the recent review by Li and Wong (2013) for additional details on the Brazilian disk technique.

Two different high-speed cameras were used to visualize the deformation and failure processes during dynamic experiments. A Kirana (Specalized Imaging) Ultra High-Speed Video Camera filming at 2 Mfps with a 110 ns exposure time captured time-resolved images of the Brazilian disk experiments, while an Ultra 8 (Hadland Imaging) camera was used to capture images of the uniaxial compression experiments at frame rates up to 1 Mfps with exposure times of 200 ns. The use of cuboidal specimens and the flat face of the Brazilian disk allows us to visualize failure.

After each test, fragments were collected and imaged using a Zeiss optical microscope with an AxioCam MRC camera. An example image showing the fragments is shown in Figure 1c. These images of fragments are converted to monochrome (Figure 1d) using a thresholding procedure, where fragments now appear as white features. An image-processing routine was used to determine the major axis dimension [1] (ℓ), projected area (A) and perimeter (P) of individual fragments. This is the same procedure used in Hogan et al. (2014). The images in Figure 1c were taken using the differential interference contrast setting (a bright-field mode) to have the fragments appear dark. Additional dark-field images with a suitable exposure were also taken to have the fragments appear in greyscale. In the greyscale images, transparent minerals such as pyroxene will show up as bright, and iron-nickel grains will show up dark. After a thresholding operation for the greyscale images, all fragments appear as white, and each white feature consists of tens of pixels. We were then able to relate the coordinates of the pixels in the monochrome to the greyscale image, and this allows us to compute the average greyscale intensity across all pixels for a given fragment in the original set of greyscale images. In turn, we relate the greyscale values to fragment

[1] The major axis dimension is taken as the largest spanning dimension of the fragment.

composition, where, again, the iron-nickel have low greyscale intensities (they are dark) and the pyroxene have high greyscale intensities (they appear bright). This operation allows for correlations between fragments size, shape and composition to be investigated. Image processing and analysis techniques was also used to determine the major axis size, number density (#/m^2), and spacing between adjacent iron-nickel grains in the initial GRO 85209 microstructure (Figure 1b). The sizes and number densities were used when exploring or strength results, while the spacing distributions are compared with fragmentation size measurements. A Tescan Mira3 GM Scanning Electron Microscope (SEM) is also used to investigate fracture surfaces, while Energy Dispersive Spectroscopy (EDS) capabilities are used to identify composition of constituent phases.

3. Dynamic Failure Experiments

In this section we examine the stress-time history and associated time-resolved high-speed photography of the dynamic failure experiments. We then examine failure surfaces of fragments using optical microscopy and scanning electron microscopy techniques to determine likely sites for crack initiation, and the dominant modes of crack propagation.

3.1. Characterization of Strength and Failure Processes

Initially we consider the time-resolved failure of a Brazilian disk experiment in Figure 3. The stress-time curve is shown as the solid black curve, which increases nearly linearly with time to a peak stress of 36 MPa at 30 μs after loading begins. This is its dynamic tensile strength at that corresponding strain rate. After the peak stress is reached, the stress decreases to zero over the next 100 μs. The stress rate $\dot{\sigma}$ is taken as the slope of a linear fit to the rising portion of the stress–time curve between 10 and

90 % of the peak stress, illustrated by the dashed-line (red underneath). For this experiment the stress rate is calculated to be 1.6 MPa/μs. The nominal strain rate may be estimated by dividing the stress rate by the Young's modulus, $\dot{\epsilon}$ =114 s^{-1} for this experiment. Due to the non-uniform deformation of the Brazilian disk samples, we cannot directly measure the strain rate using the classic Kolsky bar equations, and so we report the stress rate and estimate the strain rate using the initial modulus. Corresponding time-resolved high-speed video images selected at 12 μs intervals (t_1 to t_6) are shown on the right of Figure 3 so as to allow the fracture to be visualized throughout the duration of the failure process. The loading direction (horizontal) is also defined for the images on the right. Red arrows are used in the images to denote fracture initiation sites that are determined by tracking the observed fractures backward in time. Often, the regions of fracture initiation appear as localized bright spots which are likely due to reflection of light from a highly reflective grain in the material that is rotating out-of-plane. In GRO 852909, bright regions are believed to be the metallic iron-nickel grains in the microstructure, which we also believe serve as the most common fracture initiation sites. Additional evidence that fracture initiates from the iron-nickel grains is shown later in optical microscope images in Figure 5a, as well as in fragmentation results presented later in Figure 9.

At peak stress (t_1) in Figure 3, no fractures are visible on the specimen surface. At 12 μs post-peak stress (t_2), there is a fracture that initiates near the middle of the sample (right arrow) and is visible spanning the middle of the disk between both arrows. The stress in the sample collapses as a result of fracturing. At 24 μs after peak stress (t_3), additional fractures are initiated from iron-nickel grains to the right of the original fracture and, as a result, the stress continues to collapse. At t_4, fractures are observed to fully span the disk surface. The spanwise propagation of the crack across the entire length of the sample may possibly relate to the hump we observe in the stress-time curve on the left just prior to t_4. It is challenging to observe additional larger fractures on the surface at later times (t_5 and t_6), although they likely occur. The stress in the sample continues to collapse to 0 MPa at these later times. The average speed of the first few cracks measured across multiple experiments is 500 ± 90 m/s, and this is measurement by tracking the displacement of the crack tip over multiple camera frames across many experiments.

Next we consider a dynamic uniaxial compression experiment in Figure 4. The stress-time curve is shown on the left, and time-resolved high-speed camera images (t_1 to t_6) are shown on the right. The numbered grey dots in the stress-time plot indicate the times and values of stress corresponding to each numbered image. Here, images are shown at 8 μs intervals. The loading of the material in the high-speed video images occurs from left to right, and red arrows are used to highlight the location of cracks in the specimen. In this experiment, the compressive strain rate was measured to be 1,000 s^{-1} as calculated from the standard Kolsky bar analysis (Ramesh, 2008). The stress time-plot indicates that the stress rises in a nearly linear manner to a peak value of 294 MPa (the uniaxial compressive strength) at ~20 μs after loading. Just before peak stress (image t_1), we see no cracks on the surface of the specimen. After the peak stress is reached cracks grow, reducing the stress in the sample. At t_2, we see one crack near the lower right surface. In subsequent images this crack continues to extend, and other cracks can be seen on the surface as indicated by the red arrows. At the time corresponding to t_4, the stress in the sample has fallen to zero, and subsequent images show that the specimen continues to fracture and expand in the vertical direction. Here we highlight bright regions that intersect the cracks using the red arrows. The average speed of cracks across multiple images has been measured to be 139 ± 64 m/s. Images of t_5 and t_6 show a multitude of cracks that have aligned with the axis of loading, as well as some additional bright regions intersecting these cracks that are believed to be iron-nickel grains. It has been documented elsewhere, that these axial cracks form columns, and at later times, these columns buckle and transverse fracturing (i.e., perpendicular to the axial cracks) occurs (Ashby and Hallam, 1986; Hogan et al., 2014). Interestingly, we also observe bright features on the surface of high-speed camera images in Fig. 10 of Kimberley and Ramesh (2011) and we see fracture intersecting these bright features. The bright spots are iron-nickel grains in MAC 88118 (also confirmed with our recent post-experiment analysis of the fragments). We believe a similar failure process occurs in our experiments of GRO 85209, and that iron-nickel grains serve as initiation sites for failure.

3.2. Fracture Initiation and Fragment Characterization

Micro-scale modes of failure are determined by examining fragments (collected from each experiment) in both optical and scanning electron microscopes. Figure 5 shows, as an example, images of fragments collected from a dynamic uniaxial compressive experiment. First we examine an optical microscope image of internal fracture features inside of a polyphase fragment (Figure 5a). To acquire this image, some fragments are mounted in resin and systematically polished through their cross-section. In the example shown in Figure 5a, exposed iron-nickel grains (highlighted by white arrows) are observed protruding from the fracture surface and there is evidence of internal fractures intersecting regions of high angularity of the iron-nickel grains (highlighted by yellow arrows). This suggests that fracture of GRO 85209 initiates from iron-nickel grains, and that compressive failure of this material results in the generation of internal damage. Stiffness and hardness mismatches between the iron-nickel grains and adjacent pyroxene grains (the lighter grain materials in Figure 5a) are believed to promote fracture at these boundaries. Here, the stiffness for pyroxene is 95±3 GPa, and for the iron-nickel 178±6 GPa (measured using nano-indentation).

Next, we examine a representative portion of fragments in the image in Figure 5b. In this image, there are two different features of fragments: 1. optically bright fragments and 2. optically dark fragments. The brighter fragments are primarily comprised of pyroxene (confirmed with scanning electron microscopy and electron dispersive spectroscopy). The brightness of the fragments appears to be dependent on their size, with smaller ones being much brighter and the larger ones being grainy. Examples of both are highlighted. They appear grainy because their surface morphology is highly variable, and they are comprised of multiple pyroxene and iron-nickel grains. We also observe iron-nickel grains protruding from the surface of the larger fragments, which is also shown in Figure 5a. The individual darker fragments in Figure 5b are iron-nickel grains (confirmed with electron dispersive spectroscopy). We see that the darker fragments are mainly around 150 μm in size, with only a few smaller ones.

We explore the surface morphology of a large fragment further in the scanning electron microscope image in Figure 5c. The fragment is mainly comprised of pyroxene and the surface is quite jagged. This is believed to be a result of transgranular fracture (Figure 5d) of the pyroxene mineral, which is believed to the dominant failure mode of this mineral due to its relative weak cleavage plane. Shown in Figure 5d is a magnified image of a region on the pyroxene fragment. In the centre of this image is an iron-nickel grain that is protruding from the surface, much like in Figure 5a and b. All together, these results highlight the character (composition) of different fragment sizes, as well as provide further evidence that iron-nickel grains play an important role in the failure process in GRO 85209.

4. Connections Between Defects and Strength

4.1. The Scaling of Rate Dependent Strength

In this section, the results of the strength measurements obtained in the previous section are compared with the rate dependent strength model of Kimberley et al. (2013). This model describes the rate dependent strength of brittle materials by incorporating fundamental physics related to crack initiation, growth, and interaction. The model is sensitive to key microstructural (e.g. flaw size) and material parameters (e.g. Young's modulus), and takes the following form:

$$\frac{\sigma_c}{\sigma_0} = 1 + \left(\frac{\dot{\epsilon}}{\dot{\epsilon}_0}\right)^{2/3}. \tag{2}$$

Here, σ_c is the compressive strength, and $\dot{\epsilon}$ is the applied strain rate. σ_0 is a characteristic compressive strength term (taken as the quasi-static compressive strength) which depends on the internal flaw distribution:

$$\sigma_0 = \alpha \frac{K_{Ic}}{\bar{s}\eta^{1/4}}, \tag{3}$$

where K_{Ic} is the mode I fracture toughness (Pa $\sqrt{m}$), $\bar{s}$ is the average flaw size (m) and η is the areal flaw density (m^{-2}). The term α is a dimensionless proportionality constant. The corresponding characteristic compressive strain rate, $\dot{\epsilon}_0$, is defined as:

$$\dot{\epsilon}_0 = \alpha \frac{v_c K_{Ic} \eta^{1/4}}{\bar{s}E} \tag{4}$$

where v_c is a limiting crack growth speed (m/s), and E is the Young's modulus (Pa). Kimberley et al. (2013) have shown that this model captures the behavior of a large number of brittle materials, including engineered ceramics and geological materials.

To compare the results of the unconfined compression experiments with this model, values of σ_0 and $\dot{\epsilon}_0$ were fit to the experimental data using the functional form of Equation (2), and are presented in Table 1. The normalized strength data are plotted in Figure 6 along with the normalized strength data for meteorite MAC 88118 (Kimberley and Ramesh, 2011). Here we see that the both sets of experimental show little variation in strength for low rates, but show a significant (2-4X) increase in strength at elevated strain rates, agreeing well with the model predictions.

Kimberley et al. (2013) also showed that the model presented in Equations (2 – 4) can be applied to tensile loading, although the characteristic stresses and strain rates will take on different values under tensile vs. compressive loading (because different flaw distributions are exercised). Thus the results of the indirect tension tests on GRO samples can also be compared with this model as shown in Figure 7. As no quasi-static indirect Brazilian disk data were available, nor were any direct tension data, we take the tensile quasi-static strength to be 1/10 of the quasi-static compressive strength. The choice of a ratio of 1/10 is motivated by tensile and compressive strengths found in the handbook by Charles (2001). The quasi-static tensile strengths are those points for $\dot{\epsilon}/\dot{\epsilon}_0$ < 1. The normalized experimental data agree well with the model, and shows an even more significant increase in strength at higher normalized rates when compared with the compressive results. This dramatic increase in strength is reflected in the lower value of characteristic strain rate shown in Table 1.

Since the characteristic stress (Equation (3)) and characteristic strain rate (Equation (4)) are expressed in terms of material properties and flaw distribution parameters, the best fit values of Table 1 can be compared with the values that would be predicted based upon measured material properties and flaw statistics. This is explored in the next subsection.

4.2. Relations Between Flaw Population and Strength

Flaw population statistics are calculated for the iron-nickel grains, which we believe to be the most important defect for our testing conditions. Note that the iron-nickel grain morphology does not resemble the slit-like flaw geometry that formed the basis of Equations (2 – 4). However, the distribution of iron-nickel grains is relevant if failure is controlled by cracks extending from these grains, as observed in Figure 5. We are interested in the average defect size $\bar{s}$ and the number of defects in a given area, denoted as η (#/m^2). We use these measured flaw statistics to explore our strength results for GRO 85209, as well as compare our strength measurements with existing measurements for another ordinary chondrite (MAC 88118) used by Kimberley and Ramesh (2011). MAC 88118 is an L5 ordinary chondrite meteorite that was studied in Kimberley and Ramesh (2011), and it contains a different microstructure than GRO 85209. For reference, we show the MAC 88118 microstructure in Figure 8a. Again, the lighter features are iron-nickel grains and the darker matrix material is primarily comprised of pyroxene. Examining the microstructure of MAC 88118 (Figure 8a) there appear to be more defects (iron-nickel grains) and some of which are much larger in size than observed in the GRO 85209 material (Figure 1b). The image processing routine previously outlined was also used to determine the size and total number of defects per area (#/m^2) for MAC 88118, allowing of the differences in microstructure to be quantified. In Figure 8c we plot the areal density of defects larger than the corresponding defect size. We use a power-law fit in the form of:

$$PL(x) = Cs^{-n} \tag{5}$$

where C and n are fitted coefficients to experimentally measured defect density data. Over the range of characterized defects (here we consider defects larger than 5 μm), GRO 85209 has fewer defects per unit area than MAC 88118, and the rate at which the defect density decreases (i.e., the magnitude of n) is greater for GRO 85209. This confirms the qualitative observation that MAC has higher flaw density.

We also characterize the defect half-sizes, defined as half of the longest spanning dimension of the iron-nickel grains in each material. Shown in Figure 8c is a probability plot of the defect half-size (s) for GRO 85209 as measured from figures similar to those in Figure 1b. The corresponding defect size distribution for the iron-nickel grains in MAC 88118 (measured from figures similar to those in Figure 8a) are shown in Figure 8d. Note here that we are only considering defects larger than 5 μm in the probability plot based on our ability to resolve the features in the optical microscope image. The probability plot is used for assessing whether or not an empirical data set (here it is the defect size) follows a given reference distribution (e.g., lognormal, normal). In a probability plot, the y-axis is scaled accordingly to make the selected reference distribution appear as a line. Differences between the reference line and the data set indicate a lack of fit. Mathematically: consider an ordered sets of data:

$$\bar{x}_{(1)}, \bar{x}_{(2)}, ...\bar{x}_{(m)} \tag{6}$$

with probability distribution functions of $g(\bar{x})$. The cumulative distribution function, $G(x)$, is given as:

$$G(x) = \int_0^x g(\bar{x})d\bar{x} \tag{7}$$

where $G(x)$ ranges between 0 and 1. From this, we are then able to compute percentile values of $G(x)$ (the 35^{th} percentile occurs when $G(x)$=0.35). If $F(y)$ is the cumulative distribution of a reference distribution (e.g., lognormal or normal) then we are able to contrast expected percentiles for both the data ($G(x)$) and reference distribution ($F(y)$). In Figures 8c and d, the defect sizes are compared against a lognormal distribution in the form:

$$f(x)_{\ell og} = \frac{1}{x\sigma_{\ell og}\sqrt{2\pi}} e^{-(log(x)-\mu_{\ell og})^2/2\sigma_{\ell og}^2} \tag{8}$$

where $\mu_{\ell og}$ and $\sigma_{\ell og}$ are the mean and standard deviation of the data's logarithm, respectively. The defect sizes are adequately described using a lognormal distribution for sizes > 10 μm, with the corresponding values of $\mu_{\ell og}$ and $\sigma_{\ell og}$ denoted in each subfigure. For reference, the mean defect size for GRO 85209 with standard error is 27.7 ± 0.4 μm, and 51.2 ± 1.9 μm for MAC 88118. The standard error is calculated by dividing the standard deviation by the square root of the number of size measurements. We provide a summary of the defect statistics and material properties in Table 2. Note that the reported crack growth speeds v_c were measured in several dynamic uniaxial compression experiments for each material (the measured tensile growth speeds for GRO were larger). Also note that defect densities are computed by taking the average areal density across 100+ images for both materials. We report the average of those values and the standard deviation in the last column of Table 2.

With the measured properties and flaw statistics for both MAC 88118 and GRO 85209, we can compare the changes in characteristic stress and strain rate with the experimentally determined best fit values shown in Table 1. Equation (3) allows for the ratio of characteristic stresses under compression for GRO 85209 and MAC 88118 to be expressed as:

$$\frac{\sigma_{0G}}{\sigma_{0M}} = \frac{K_{IcG}}{K_{IcM}} \frac{\bar{s}_M}{\bar{s}_G} \left(\frac{\eta_M}{\eta_G}\right)^{1/4}. \tag{9}$$

Here the subscripts G and M correspond to the properties of GRO 85209 and MAC

88118, respectively. Using the properties listed in Table 2 and assuming that the fracture toughness of the two materials are equal (there exist no measurements of fracture toughness for stony meteorites) we calculate $\sigma_{0G}/\sigma_{0M} = 1.49$. This compares reasonably with the ratio of the experimental best fit values, 1.82.

The ratio of characteristic rates is derived from Equation (4) to be

$$\frac{\dot{\epsilon}_{0G}}{\dot{\epsilon}_{0M}} = \frac{K_{IcG}}{K_{IcM}}\frac{c_G}{c_M}\frac{E_M}{E_G}\frac{\bar{s}_M}{\bar{s}_G}\left(\frac{\eta_G}{\eta_M}\right)^{1/4}. \tag{10}$$

Using the values listed in Table 2 we find the ratio of characteristic strain rates $\dot{\epsilon}_{0G}/\dot{\epsilon}_{0M} = 0.52$, which compares well with the ratio of observed values, 0.75. If we assume that the ratio of fracture toughnesses is $K_{IcG}/K_{IcM} = 1.22$ then the ratio of characteristic stresses can be forced into agreement. Our predicted ratio of characteristic rates would then equal 0.63, in closer agreement with our best fit ratio. The above calculations indicate that the strength model presented in Equations (2–4) is capable of capturing the experimentally observed trends (i.e., higher characteristic strength, and lower characteristic rate in GRO 85209) based upon difference in microstructure and material properties.

5. The Role of Microstructure on Dynamic Fragmentation

In this section we explore the effect of the microstructure's composition and defect population on the fragmentation of GRO 85209 for both stress-states we previously studied. This is mainly accomplished using the image processing techniques previously outlined to measure fragment size and mean greyscale intensity, as well as the spacing between the iron-nickel grains.

5.1. Fragment Size and Defect Spacing Distributions

Cumulative distributions of fragment sizes from GRO 85209 are shown in Figure 9 for both the quasi-static (red dashed line) and dynamic (red solid line) uniaxial compression experiments, and a lower rate and higher rate for the Brazilian disk experiments (blue lines). Note that some uncertainty exists for fragments <30 μm as these fragments are challenging to collect after the experiments. For this reason, we do not include them the analysis. Initially, we discuss the quasi-static uniaxial compression experiment (dashed red line in Figure 9). The strain rate here is 10^{-3} s^{-1}. Most of the fragments are between 30 μm and 1 mm in size, and the cumulative distribution shows an inflection at around 120 μm. We believe that this suggests that two different fragmentation mechanisms may be present. As the eCDF represents the relative frequency, we note that about 33 % of the fragments generated by quasi-static uniaxial compression are less than 120 μm in size. The cumulative distribution of fragment sizes for the dynamic uniaxial compression case is shown using the solid red curve. The strain rate here is 10^{+3} s^{-1}. The curve is shifted to the left compared to the uniaxial case, indicating that increasing the strain rate produces smaller fragments. This is due to additional internal strain energy at the peak stress (due to higher rate), and this energy is subsequently converted into more fractures (hence smaller fragments). Additionally, more defects may be activated at higher rates, thus facilitating increased fracturing and fragmentation. Also note that the bump at around 120 μm in size persists, but is less prominent. We see that about 57 % of the fragments generated in dynamic uniaxial compression are less than 120 μm in size. We divide the distributions by fragment size at a size of 120 μm, with the domain ℓ_i<120 μm called fragmentation Regime 1, and that with ℓ_i>120 μm called Regime 2.

Next, we examine the cumulative distribution of fragment sizes for two Brazilian disk experiments, one at a strain rate of 45 s^{-1} and one at 285 s^{-1}. Note again, that the deformation in the Brazilian disk tests is quite non-uniform (not pure tension), and this likely results in a different sequence of events leading to the eventual fragmentation of the sample. As before, the curves shift to left as the strain rate is increased, with Regime 1 representing 37 % of the total fragment population for the 45 s^{-1} case and 60 % for the 285 s^{-1} experiment. The inflection at around 120 μm exists for these materials as well.

Why are there two regimes of fragmentation and what is the significance of the inflection at around 120 μm? In Figure 9, we also plot the cumulative distribution of spacings between the iron-nickel grains (solid black curve) and observe that the maximum defect spacing appears to coincide with the inflection at 120 μm. There are a total of 6,200 measurements taken, so we believe the curve is representative of the actual data. We believe that this suggests that fragments $< 120\ \mu$m (Regime 1) are controlled by the microstructure defect spacing. In this mechanism, fractures initiated at the iron-nickel grains may coalesce with fractures initiated from adjacent iron-nickel grains.

5.2. Fragment Composition

In this last subsection, we investigate measurements of the mean greyscale intensity (GI) of fragments in the scatter plots of GI plotted against fragment sizes in Figure 10. In order to estimate a mean greyscale intensity, pixel values in monochrome images obtained through thresholding are related to pixel values in the original greyscale images, and the values are then averaged over the entire fragment. We normalize the mean greyscale intensity by the maximum to have the values range between 0 and 1. We show the Brazilian disk experiment at a strain rate of 285 s^{-1} in Figure 10a. Again, we only consider fragments $> 30\ \mu$m. In Figure 10a, we divide concentrations of points in the scatter plot into three sub-regions: Sub-region A, with fragments less than 120 μm in size and > 0.4 in GI that are primarily optically bright, which are believed to be comprised of pyroxene fragments (Figure 5b); sub-Region B, with fragments larger than 120 μm and GI larger than 0.4, which are polygrain and polyphase in nature and contain multiple grains of iron-nickel and pyroxene grains (Figure 5a); sub-Region C, with fragments with GI less than 0.4, i.e., dark in color, which are believed to be individual iron-nickel grains (Figure 5b). Although the bounds are drawn for all fragments sizes for sub-Region C, there appears to be a cluster of fragments that are between 70 and 180 μm. Iron-nickel grains larger than 70 μm represent 25 % of the total iron-nickel grain population. Similar sub-region trends are observed for the dynamic uniaxial compression case, which is shown in Figure 10b, although with different concentrations for each sub-region.

The total percentage (%)-representation of each sub-region to the total population is computed in Table 3. There is only one set of measurements for each of the strain rates (low and high) and stress states (Brazilian disk and uniaxial compression). We associate the uncertainty with each %-population measurement with the choice of boundaries. As examples, the bounds for the % population in sub-Region A is obtained by considering the population for all fragments less than 110 (minimum), or less 130 μm (maximum). For sub-regions B and C, we vary the size bounds between 110 and 130, and the color bounds between 0.35 and 0.45, and compute the associated % population in Table 3. The associated uncertainty is about ± 2 % for any of the measurements. From Table 3, there is an increase in the total %-representation of sub-Region A (pyroxene fragments) for increasing strain rate, and that the %-representation of sub-Region A for the Brazilian disk experiments is greater than for the uniaxial compression experiments. The %-representation of sub-Region C (iron-nickel grains) decreases as the strain rate is increased, and, again, the Brazilian Disk experiments have a greater %-representation for sub-Region C than the uniaxial compression experiments.

6. Summary and Implications

During failure, stored strain energy is converted to kinetic energy and surface energy, tensile stresses are created, and fragmentation ensues via crack growth and coalescence. In this study we have shown that the resulting fragment characteristics (sizes and composition) are dependent on where cracks are initiated, how cracks grow and branch, and how they coalesce. In GRO 85209, we believe that fractures are commonly initiated at the iron-nickel grain boundaries during dynamic compressive loading, likely a result of the stiffness mismatches between iron-nickel and pyroxene. Here, the stiffness for pyroxene is 95±3 GPa, and for the iron-nickel 178±6 GPa (measured using nano-indentation).

As these cracks grow, their pathes will be dependent on the material composition and grain boundary relationships, and the strain-rate and stress-state. In GRO 85209, scanning electron and optical microscopy identified transgranular fracture as the dominant fracture mechanism in pyroxene, while intergranular fracture was observed to dominate in the metallic iron-nickel phases. As the strain rate is increased, we expect more small fragments to be formed due to added strain energy associated with the strength increase (see Figure 6), and this manifests as a shift to the left in the cumulative distribution curves. We may also expect less intergranular fracture and more transgranular fracture. We observe this trend in the fragmentation composition results, where pyroxene represents a larger number in the total fragment population as the strain rate is increased for both materials. Similarly, as the stress-state becomes more multidimensional and non-uniform, we expect there to be more transgranular fracture than intergranular fracture. The comparison between the compression and Brazilian disks tests indicate that pyroxene represents more of the population in Brazilian disk case, perhaps a result of increased transgranular fracture. All together, fragmentation appears to be dependent on the strain-rate and stress-state, the time-history of fractures (i.e., what happens first), and the mineral compositions being fractured.

After growth at a finite crack speed, the fractures will eventually coalesce. Crack propagation speeds for the Brazilian disk test were observed to be more than 3x greater than in the uniaxial compression case (500 ± 90 m/s vs. 139 ± 64). This is, perhaps, a result of less tortuous paths experienced by the crack during loading in the Brazilian disk experiment. Fracture coalescence is also different for both stress-states studied here. In the Brazilian disk experiment, fractures are first observed to grow horizontally across the disk, and this partitions the disks into two hemispheres. At later times, the edges of the disk in contact with the platens break and this creates the fragments. In the compression case, many axial cracks are observed to propagate across the sample. At later times, these axial cracks span the entire sample, creating columns, and these columns buckle at later times, resulting in transverse fracturing (Hogan et al., 2014). The differences in structural failure likely manifest in the different fragmentation results.

After cracks are formed during structural failure, additional abrasion between surfaces is believed to generate the smaller fragments (pyroxene in composition) and individual iron-nickel grain fragments. With this sequence of events in mind, we summarize the key fragmentation regions as follows:

1. Sub-Region A: This fragmentation mechanism is associated with the initiation, propagation and coalescence of fractures between iron-nickel grains. Fragments in this regime are less than 120 μm in size, and are primarily comprised of pyroxene fragments, which is the weakest mineral phase and the matrix material

in GRO 85209. Weaker materials are preferentially comminuted during high-rate events (Spray, 2010). We associate the increase in %-representation of the smaller pyroxene fragments (sub-Region A) for increasing strain rates (independent of stress-state) as a result of the additional strain energy in the sample and the subsequent increase in the number of activated defects. Smaller fragments being composed in the matrix material was also noted by Durda and Flynn (1999) and Flynn and Durda (2004), and the has implications in the collection of interplanetary dust particles (believed to originate from the asteroid belt), where they note that the smallest fragments composition may not be wholly representative of the parent material (e.g., in terms of volatile content).

2. Sub-Region B: Fragments in this region are greater than 120 μm in size, and polyphase and polygrain in character. These are developed through failure mechanisms that occur during the structural failure of the sample. The mechanisms activated during failure are dependent on the geometry, loading history, stress-state, and strain-rate. In uniaxial compression, failure occurs through the coalescence of axial and transverse cracks (Horii and Nemat-Nasser, 1985). In the Brazilian disk experiment, multiple horizontal cracks first grow across the sample to partition the disk into two hemi-disks, and at later times the hemi-disks fracture.
3. Sub-Region C: Fragments in this regime are comprised of individual iron-nickel grains that are between 60 and 200 μm in size. We believe these fragments are too ductile to easily fracture again.

Similar links between the microstructure and fragmentation have been noted by Durda and Flynn (1999), wherein fragment sizes were noted to be related to matrix materials or individual grains. In their case, the chondrules dominate the failure sites during impact in a meteorite materials, whereas in our case its the iron-nickel grains.

Lastly, the boundary between both the microstructure- and structural-dependent fragmentation regimes (≈120 μm) is less distinct in this material than in the advanced ceramic boron carbide (Hogan et al., 2014), where a clear separation exists for fragments between 70 and 100 microns in size. This can be possibly explained as follows: the lower bound of the structural controlled fragmentation (Regime 2) is related to the energy that is available to fragment the body through axial and transverse cracking (in the case of compression). One could essentially view this regime as those described by the rate-dependent brittle fragmentation models that exist in the literature (e.g., Grady (2006), Glenn and Chudnovsky (1986), Zhou et al. (2006a), and Levy and Molinari (2010)). On the other hand, the upper bound of the microstructure regime is believed to correspond to the upper bound of the spacing distribution. Certainly, energy is also required to create these fragments as well, but the mechanism is different. As the strain rate is increased, more and more defects are probed, so more of the spacing distribution is probed. For some sufficiently high strain rate, the microstructure-dependent and structural-dependent mechanisms will begin to overlap over a certain size range as they compete against each other. For boron carbide, the characteristic strain rate in compression is approximately 10^4s^{-1}, whereas the characteristic strain rate in compression for GRO 85209 is 150s^{-1}. Thus, at a comparable testing strain rate (≈10^3s^{-1}), one would expect the failure and fragmentation of the GRO 85209 to be more catastrophic (since the rate is well-beyond where it exhibits strain-rate dependence), and thus perhaps more overlap between the regimes is to be expected.

6.1. Implications

Insights gained from the experimental strength and fragmentation results have implications in the generation of regolith and catastrophic disruption. The fragmentation results and past studies indicate that fragment sizes in an impact event will be dependent on defect populations (links made here) and mechanical properties (Grady, 1982). The crack speed is also influential in the fragmentation process. Crack speeds in this ordinary chondrite (GRO 85209: 139 ±64) are lower than those reported by Hogan et al. (2015) for basalt (650 ± 100), mainly due to the added porosity and increased plasticity in GRO 85209. This will have consequences in fragmentation outcomes, where the relatively lower crack speeds would result in smaller fragments for the ordinary chondrite than a basaltic material (since fragment size is proportional to crack speed multiplied by a time). This has two implications: (1) finer regolith would be generated on bodies composed of ordinary chondrite (compared to basalt), and the ordinary chondrite would be harder to disrupt than a basaltic (since it is more challenging to yield larger enough fragments). Experimental evidence to both is found in Cintala and Hörz (2008). Additional consideration of the influence of crack speed, mechanical properties, and defect populations may also be important in interpreting regolith formation on planets (e.g., lunar mare vs. highlands). For the lunar mare (mainly basaltic), results from this paper and Hogan et al. (2015) will provide insight into its failure and fragmentation mechanisms. The interpretation of fragmentation from the highlands may be different, since it is mainly comprised of anorthosite (a monophase material), and the key defects and crack speeds are not yet well understood in this material.

Additionally, the functional form of Equation (4) yields some insights into what happens during repeated impacts. Equation (4) predicts that the characteristic strain rate is proportional to the quarter root of the areal flaw density, and inversely proportional to the flaw size. Under the action of many impacts that are not severe enough to cause fragmentation, some cracks within the body will be activated, grow and eventually link up, resulting in an increase in the flaw sizes in the body (and perhaps a net decrease in the number of flaws as a result of the linkup). A net increase in defect size and defect density would result in a decrease in the characteristic strain rate of the material (according to equation (4), and thus the material would be harder to disrupt. The consequence of repeated impacts can also evolve the net defect population (identified as microstructural heterogeneities *as well as* the newly introduced cracks) in other ways (both in terms of net defect density and the shape of the distribution. In turn, the characteristic strain rate may change leading perhaps to changes in the effective dynamic strength of the material.

Lastly, the direct link between microstructure (e.g., composition, defect spacing) and fragmentation also has implications for developing analytical models to predict the size of regolith on airless bodies through mechanical fragmentation (e.g., fragmentation models by Grady (1982); Glenn and Chudnovsky (1986); Zhou et al. (2006b); Levy and Molinari (2010)). In the current study we showed that there are two fragmentation mechanisms associated with the failure of GRO 85209: a mechanism associated with the structural failure, and a mechanism associated with the microstructure. Our results indicate that the microstructure-controlled mechanism becomes more important for increasing rate and for increasingly complicated stress-states. We hypothesize that the rates and stress-states that manifest during impact would tend to favor microstructure-dominated fragmentation. In the recent review paper by Ramesh et al. (2015), the current (essentially structural) models by Grady (1982); Glenn and Chudnovsky (1986); Zhou et al. (2006b); Levy and Molinari (2010) were shown to *over-estimate* the average fragment size in uniaxial compression tests of basalt. This suggests that these analytical models may not be sufficient to predict the fragmentation size outcomes of impact events (e.g., regolith generation) on basaltic bodies like the moon. New models are needed that include microstructure, allowing one to more fully understand how fragmentation evolves during impact for different materials (e.g., lunar mare vs. highlights). In addition, we also note that the analytical models of Grady (1982); Glenn and Chudnovsky (1986); Zhou et al. (2006b); Levy and Molinari (2010) are developed for a tensile stress-state, and new models are also needed for compression. Further challenges exist in the description and prediction of size distribution shapes (like those shown in Figure 9), and incorporation of the activation of additional failure mechanisms into the fragmentation models that depend on the loading history (Ramesh et al., 2015)

7. Concluding Remarks

We have examined microstructure and stress-state effects on the strength, failure and fragmentation of an ordinary chondrite (GRO 85209). The iron-nickel grains have been identified as sites for fracture initiation during dynamic uniaxial compression and indirect dynamic tension (using the Brazilian Disk technique). The size and number per area of the iron-nickel grains were then quantified, and in conjunction with a recently developed scaling relation, they were used to explore our experimental results, as well as the differences in strength between the ordinary chondrite in this paper and another study by Kimberley and Ramesh (2011). Fragments were also collected after the experiments, and measurements of their size, shape, and greyscale intensity were used to inform us about inherent failure and microstructural lengths that are probed during our loading conditions. Two fragmentation mechanisms were identified: one associated with the structural failure of material and one associated with inherent microstructure length scales (i.e., size and spacing of defects). Understanding the role of defects on the strength, failure and fragmentation of representative extra-terrestrial materials is central for developing improved numerical models of naturally-occurring planetary and space science phenomena (e.g., regolith generation).

8. Acknowledgment

This material is based upon work supported by the National Aeronautics and Space Administration under grant NNX09AE39G issued through the Planetary Geology and Geophysics. This work was also supported by the Solar System Exploration Research Virtual Institute (SSERVI) NASA Cooperative Agreement NNA14AB02A for the Volatiles, Regolith and Thermal Investigations Consortium for Exploration and Science (VORTICES). The authors thank Dr. Tim McCoy and Dr. Linda Welzenbach at the Smithsonian Institute for providing the meteorite samples and performing the chemical composition analysis. Bruce Marsh is thanked for many discussion on behavior of geological materials. Joey Tilson, Joe Hajj, and Nicole Cade-Ferreira are thanked for their help during experimentation and data collection.

9. References

Ashby, M., Hallam, S., 1986. The failure of brittle solids containing small cracks under compressive stress states. Acta Metallurgica 34 (3), 497 – 510.

Charles, A., 2001. Handbook of ceramics, glasses, and diamonds.

Cintala, M. J., Hörz, F., 2008. Experimental impacts into chondritic targets, part i: Disruption of an l6 chondrite by multiple impacts. Meteoritics & Planetary Science 43 (4), 771–803.

Dombard, A. J., Barnouin, O. S., Prockter, L. M., Thomas, P. C., 2010. Boulders and ponds on the asteroid 433 eros. Icarus 210 (2), 713–721.

Durda, D. D., Flynn, G. J., 1999. Experimental study of the impact disruption of a porous, inhomogeneous target. Icarus 142 (1), 46–55.

Flynn, G. J., Durda, D. D., 2004. Chemical and mineralogical size segregation in the impact disruption of inhomogeneous, anhydrous meteorites. Planetary and Space Science 52 (12), 1129–1140.

Glenn, L. A., Chudnovsky, A., Feb. 1986. Strain and energy effects on dynamic fragmentation. Journal of Applied Physics 59 (4), 1379 –1380.

Grady, D. E., 1982. Local inertial effects in dynamic fragmentation. Journal of Applied Physics 53 (1), 322–325.

Grady, D. E., 2006. Fragmentation of rings and shells: the legacy of N.F. Mott. Springer.

Grossman, J. N., 1994. The meteoritical bulletin, no. 76, 1994 january: The u.s. antarctic meteorite collection*. Meteoritics 29 (1), 100–143.

Hogan, J., Plescia, J., El Mir, C., Ramesh, K., Apr. 2015. Dynamic brittle fragmentation: Probing the byproducts of hypervelocity impact in space. In: 2015 Hypervelocity Impact Symposium (HVIS 2015). Boulder, USA.

Hogan, J. D., Farbaniec, L., Shaeffer, M., Ramesh, K., 2014. The effects of microstructure and confinement on the compressive fragmentation of an advanced ceramic. Journal of the American Ceramic Society.

Holsapple, K. A., 2 2009. On the ”strength” of the small bodies of the solar system: A review of strength theories and their implementation for analyses of impact disruptions. Planetary and Space Science 57 (2), 127–141.

Horii, H., Nemat-Nasser, S., 1985. Compression-induced microcrack growth in brittle solids: Axial splitting and shear failure. Journal of Geophysical Research: Solid Earth (1978–2012) 90 (B4), 3105–3125.

Hörz, F., Cintala, M., 1997. The barringer award address presented 1996 july 25, berlin, germany: Impact experiments related to the evolution of planetary regoliths. Meteoritics & Planetary Science 32 (2), 179–209.

Housen, K. R., Holsapple, K. A., 1999. Scale effects in strength-dominated collisions of rocky asteroids. Icarus 142 (1), 21 – 33.

Hu, G., Liu, J., Ramesh, K. T., 2014. A 3d mechanistic constitutive model of brittle materials containing evolving flaw distributions under dynamic multiaxial loading. Journal of the Mechanics and Physics of Solids under review.

Kimberley, J., Ramesh, K. T., 2011. The dynamic strength of an ordinary chondrite. Meteoritics & Planetary Science 46 (11), 1653–1669.

Kimberley, J., Ramesh, K. T., Daphalapurkar, N. P., 2013. A scaling law for the dynamic strength of brittle solids. Acta Materialia 61 (9), 3509 – 3521.

Levy, S., Molinari, J., 2010. Dynamic fragmentation of ceramics, signature of defects and scaling of fragment sizes. Journal of the Mechanics and Physics of Solids 58 (1), 12 – 26.

Li, D., Wong, L., 2013. The brazilian disc test for rock mechanics applications: Review and new insights. Rock Mechanics and Rock Engineering 46 (2), 269–287.

Michel, P., Benz, W., Richardson, D. C., 2003. Disruption of fragmented parent bodies as the origin of asteroid families. Nature 421 (6923), 608–611.

Paliwal, B., Ramesh, K. T., McCauley, J. W., Chen, M., 2008. Dynamic compressive failure of alon under controlled planar confinement. Journal of the American Ceramic Society 91 (11), 3619–3629.

Ramesh, K., Hogan, J. D., Kimberley, J., Stickle, A., 2015. A review of mechanisms and models for dynamic failure, strength, and fragmentation. Planetary and Space Science 107, 10–23.

Ramesh, K. T., 2008. High strain rate and impact experiments. In: Sharpe Jr., W. (Ed.), Springer handbook of experimental solid mechanics. Springer, Berlin, Ch. 33, pp. 929–960.

Ruiz, G., Ortiz, M., Pandolfi, A., 2000. Three-dimensional finite-element simulation of the dynamic brazilian tests on concrete cylinders. International Journal for Numerical Methods in Engineering 48 (7), 963–994.

Ryan, E. V., 2000. Asteroid fragmentation and evolution of asteroids. Annual Review of Earth and Planetary Sciences 28 (1), 367–389.

Spray, J. G., 2010. Frictional melting processes in planetary materials: From hypervelocity impact to earthquakes. Annual Review of Earth and Planetary Sciences 38 (1), 221–254.

Swab, J. J., Yu, J., Gamble, R., Kilczewski, S., 2011. Analysis of the diametral compression method for determining the tensile strength of transparent magnesium aluminate spinel. International journal of fracture 172 (2), 187–192.

Zhang, Q., Zhao, J., 2013. A review of dynamic experimental techniques and mechanical behaviour of rock materials. Rock Mechanics and Rock Engineering, 1–68.

Zhou, F., Molinari, J. F., Ramesh, K., 2006a. Analysis of the brittle fragmentation of an expanding ring. Computational Materials Science 37 (1-2), 74 – 85.

Zhou, F., Molinari, J. F., Ramesh, K. T., 2006b. Effects of material properties on the fragmentation of brittle materials. International Journal of Fracture 139, 169–196.

List of Tables

List of Figures

Table 1: Estimates for the characteristic stress (σ_0) and the characteristic strain-rate ($\dot{\epsilon}_0$) that provide the best fit of the experimental data to the strength model.

Material	Stress state	σ_0 (MPa)	$\dot{\epsilon}_0$ (s^{-1})
MAC 88118	Compression	50	200
GRO 85209	Compression	91	150
GRO 85209	Tension	10	35

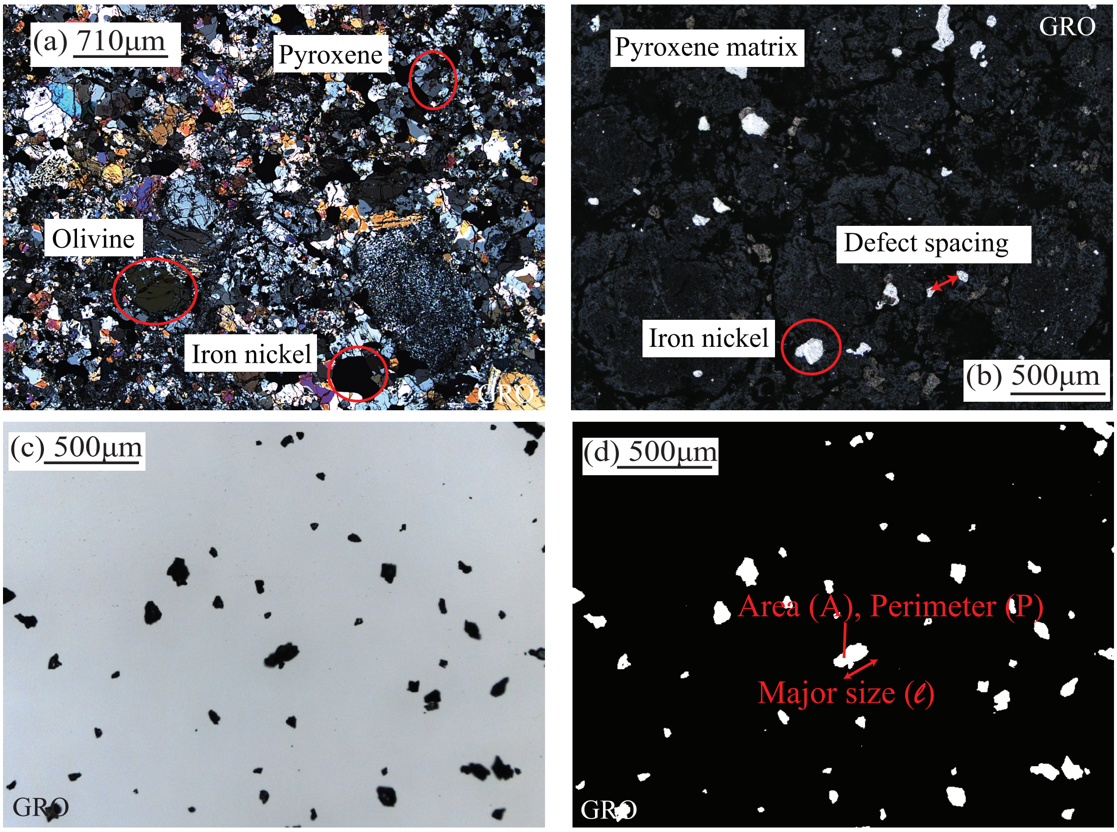

Fig. 1: (a) Polarized optical microscope image of GRO 85209 thin section (credit: Linda Welzenbach, Smithsonian Institute) and (b) non-polarized surface image of GRO 85209 microstructure, both with constituent phases labelled. In this study we are interested in linking the size and number per unit area of the iron-nickel grains, and the spacing between these grains with strength, failure and fragmentation results. (c) Optical microscope image of GRO 85209 fragments and (d) converted monochrome image with fragment statistics defined.

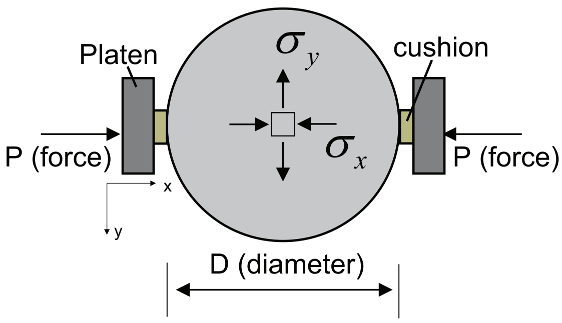

Fig. 2: Schematic of Brazilian Disk experiment with tensile stress (σ_y) labelled.

Table 2: Material properties and defect characteristics for GRO 85209 and MAC 88118, including: Young's modulus (E: Pa), density (ρ: kg/m^3), crack speed (v$_c$: m/s), average defect size with standard error ($\bar{s}$:μm), and defect density with standard deviation (η: #/m^2).

Material	E GPa	ρ kg/m^3	v$_c$ m/s	$\bar{s}$ μm	η (s>5 μm) #/m^2
GRO 85209	14	3,350	139 ± 64	27.7 ± 0.4	3.5 ± 1.1 $\times 10^7$
MAC 88118	3.2	3,240	136 ± 60	51.2 ± 1.9	7.8 ± 2.5 $\times 10^7$

Table 3: Percentage-contribution of sub-Regions A-C for uniaxial (UC) and indirect tension using Brazilian disk testing (BD). The uncertainty in each measurement is about ±2%

sub-Region	UC at 10^{-3} s^{-1}	UC at 10^{+3} s^{-1}	BD at 45 s^{-1}	BD at 285 s^{-1}
A: Pyroxene-dominated	33	57	37	60
B: Polyphase and Polygrain	45	25	27	8
C: Iron-Nickel-dominated	22	18	36	32

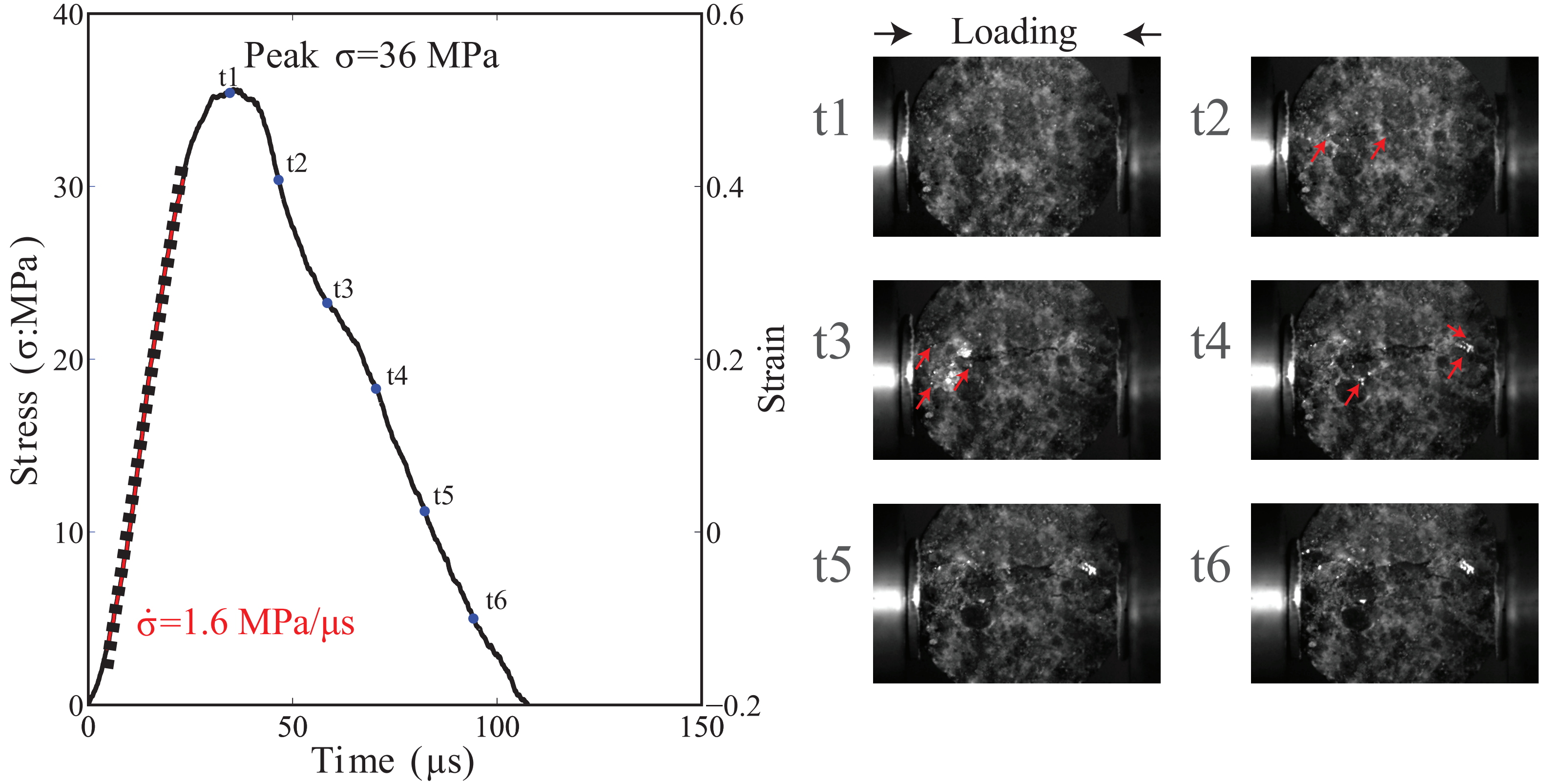

Fig. 3: Stress-time history of dynamic Brazilian disk experiment of GRO 85209 (left) with time-resolved high-speed video images showing mesoscale failure mechanisms (right). The hashed line in the stress-time plot is the linear fit of 10 and 90 % of the peak stress and this corresponds to a stress rate of $\dot{\sigma}$=1.6 MPa/μs.

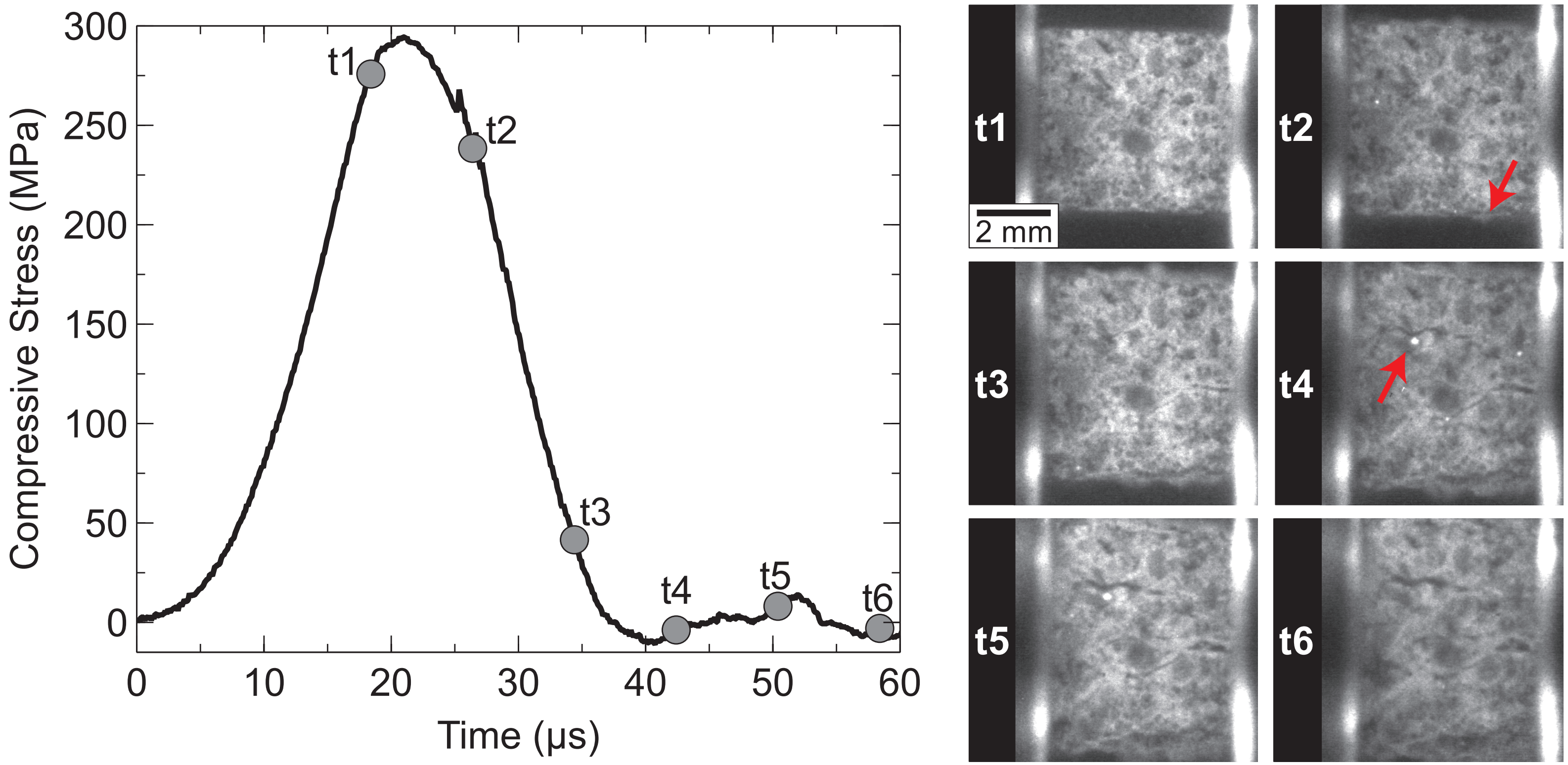

Fig. 4: Stress-time history of dynamic uniaxial compression of GRO 85209 (left) with time-resolved high-speed video images showing mesoscale failure mechanisms (right).

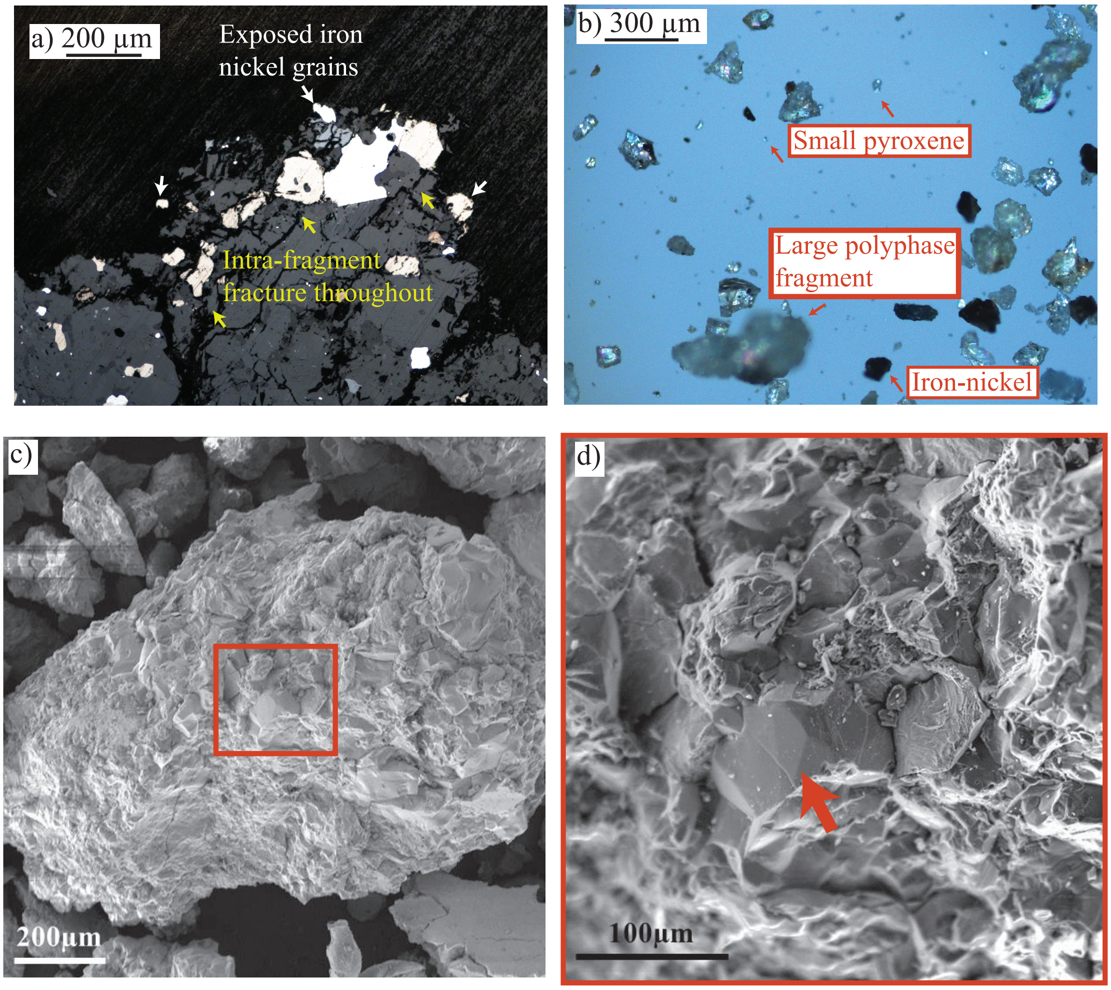

Fig. 5: GRO 85209 optical microscope images of: (a) internal fracture features inside of fragments, (b) the character of fragments showing optically bright (pyroxene) and dark (iron-nickel) phases, as well as combinations (polyphase and polygrain). (c) Scanning electron microscope image of a pyroxene fragment with (d) highlighted region of an iron-nickel grain protruding from the surface of the pyroxene fragment.

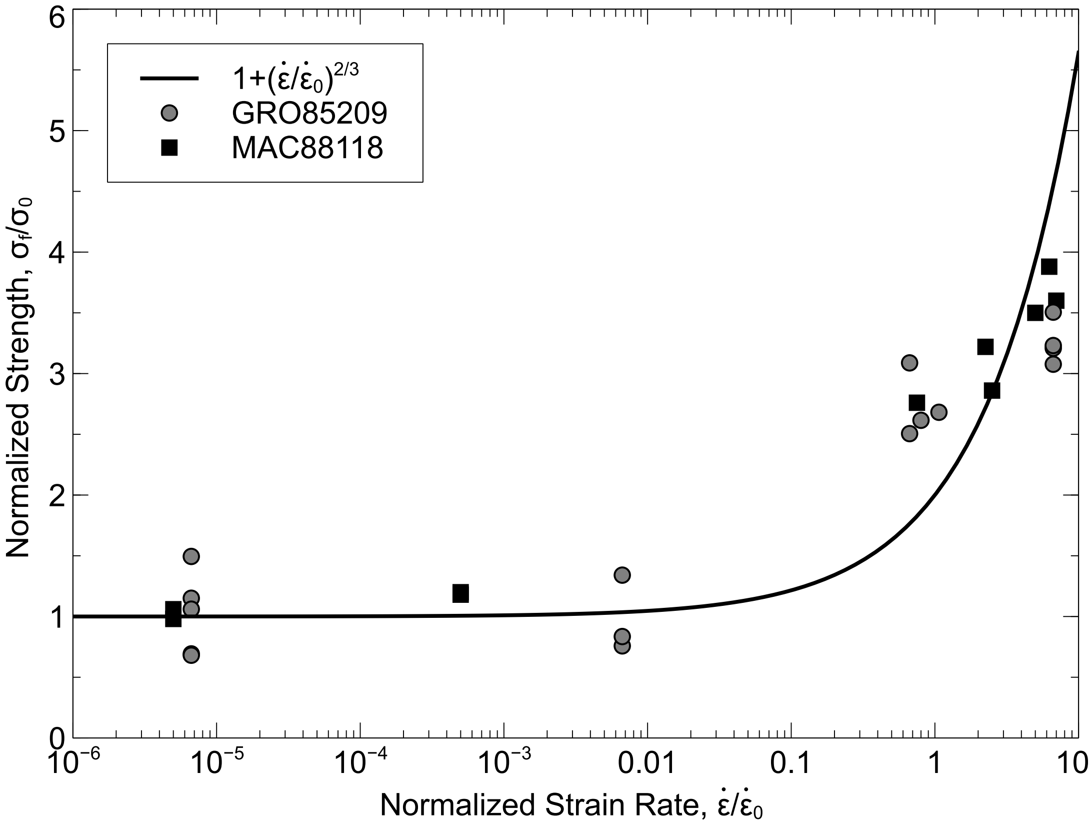

Fig. 6: Normalized uniaxial compressive strength data for MAC 88118 and GRO 85209 samples compared with the strength model of Kimberley et al. (2013).

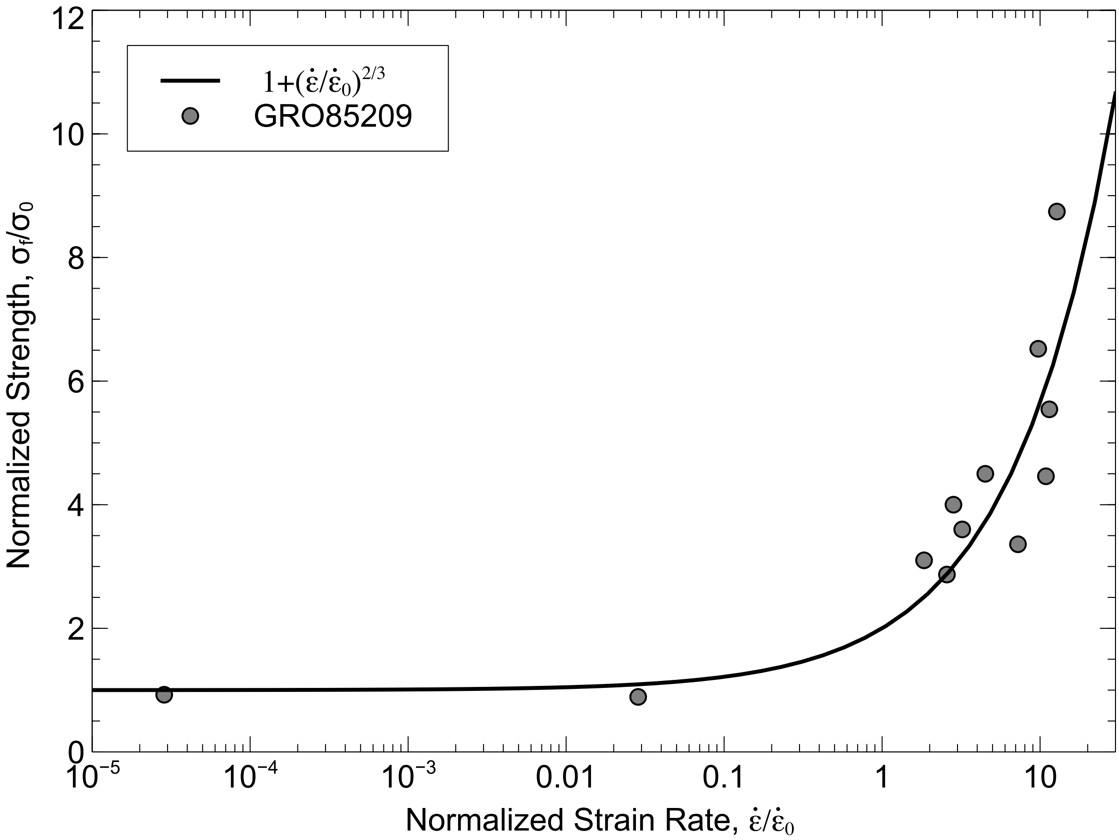

Fig. 7: Normalized indirect tensile strength data for GRO 85209 samples compared with the strength model of Kimberley et al. (2013).

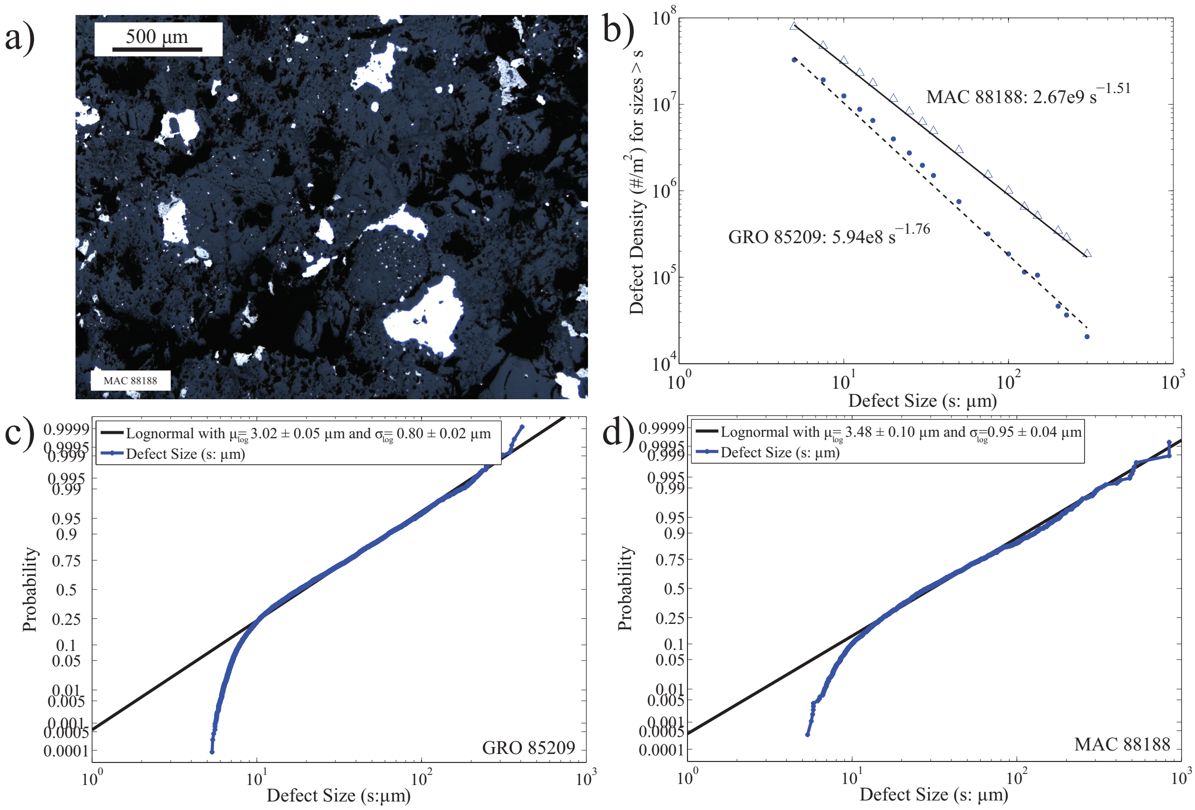

Fig. 8: (a) Optical microscope image of MAC 88118 microstructure, (b) Iron-nickel defect areal number density (#/m^2) for all defects larger than the corresponding size on the x-axis. Probability plot of defect size (s) comparing experimentally measured sizes with exponential distribution for (c) GRO 85209 and (d) MAC 88118.

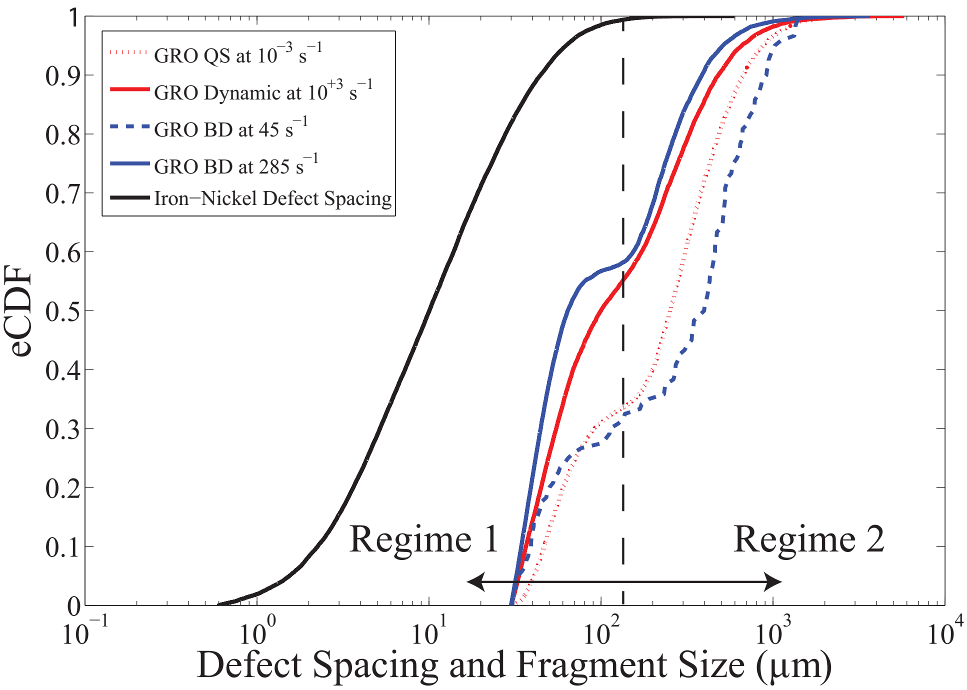

Fig. 9: GRO 85209: cumulative distribution of fragment major axis sizes and spacing between iron-nickel grains for uniaxial compression and in-direct tension using the Brazilian disk tests. Strain rates are labelled.

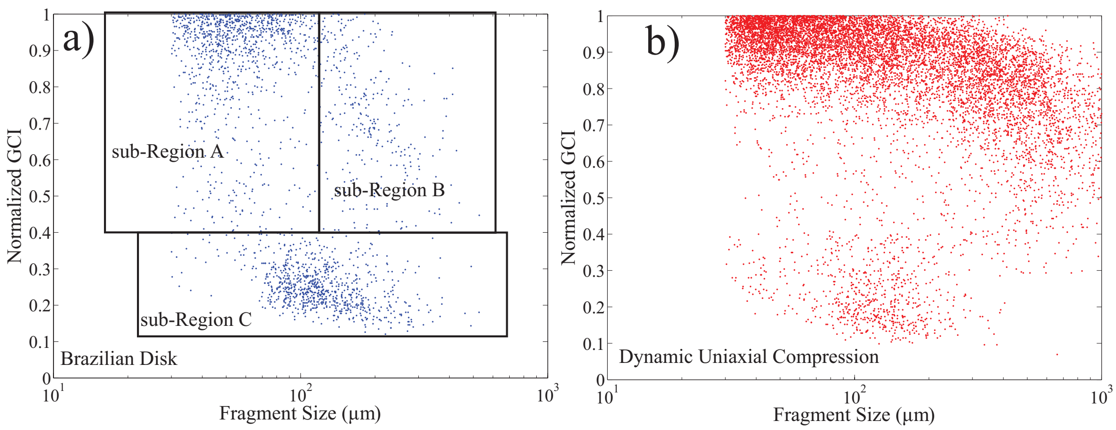

Fig. 10: GRO 85209: mean greyscale color intensity (CGI) for: (a) Brazilian Disk experiment at a strain rate of 285 s^{-1} and (b) uniaxial compression experiment at a strain rate of 10^{+3} s^{-1}.